Stochastic template banks for GW searches using low-discrepancy sequences

Tarun Kumar and Anand S. Sengupta

Dept. of Physics, Indian Institute of Technology Gandhinagar, Gujarat 382055, India.

E-mail: kumar.tarun@alumni.iitgn.ac.in, asengupta@iitgn.ac.in

Abstract. Matched filtering remains the most sensitive method for detecting gravitational waves from compact binary coalescences. The efficiency of such searches depends on how well a discrete template bank covers the underlying parameter space. Conventional geometric, stochastic, and hybrid placement methods can lead to uneven coverage and redundant templates in higher dimensions. Hybrid methods are generally the most efficient among these, while stochastic methods are simpler to implement, particularly when the parameter-space metric is difficult to compute. In practice, both approaches rely on uniform random sampling, which often requires a large number of proposal points to achieve adequate coverage. We find that stochastic template banks constructed using low-discrepancy sequences achieve comparable recovery fractions while requiring 27.5% fewer proposal points in two dimensions and 12% fewer in three dimensions. The final template count changes only marginally ($\sim 1\%$), consistent with the metric-volume constraints of the covering problem. The primary benefit of low-discrepancy sampling is therefore a reduction in the size of the initial proposal set, leading to lower memory usage and reduced bookkeeping during bank generation. Since the final template count is governed mainly by the metric volume of the target parameter space, the wall-clock speed-up is more modest than the reduction in proposal count. Nevertheless, low-discrepancy sampling provides a simple and scalable improvement to stochastic template-bank generation for current and future gravitational-wave searches.

arXiv:2607.18633v1 [gr-qc] 21 Jul 2026

1. INTRODUCTION

Gravitational waves (GWs) are propagating perturbations of spacetime generated by accelerating mass distributions, with compact binary coalescences among their most prominent astrophysical sources. Owing to the weak coupling of gravity to matter, the strains induced by astrophysical GWs at terrestrial detectors are typically extremely small, necessitating highly sensitive interferometric observatories, including LIGO [1], Virgo [2], and KAGRA [3]. The first direct detection of gravitational waves, GW150914 [4], observed by the two LIGO detectors, marked the beginning of gravitational-wave astronomy. The signal was attributed to the inspiral and merger of a spinning binary black hole system with inferred source-frame component masses of $36^{+5}_{-4}\,M_\odot$ and $29^{+4}_{-4}\,M_\odot$ [4] respectively.

From the first observing run (O1) through the second part of the fourth observing run (O4b), the cumulative GWTC-5.0 catalog [5] contains 390 compact-binary coalescence

candidates with $p_{\rm astro} \geq 0.5$, where $p_{\rm astro}$ [6] is the inferred probability that a candidate is of astrophysical origin rather than terrestrial noise.

Looking ahead, the detection rate is expected to grow significantly with next-generation observatories such as LISA [7], the Einstein Telescope [8], and Cosmic Explorer [9], whose enhanced low-frequency sensitivity will extend the observable horizon and enlarge the accessible source population. The addition of LIGO-India [10, 11] will further strengthen the ground-based detector network by improving detection efficiency and source localization capabilities [12], while proposed decihertz mission concepts such as IndIGO-D [13] could enable multiband observations and early-warning localization of compact binary coalescences.

The detection of gravitational waves from coalescing compact binaries [14] relies on matched filtering [15–17], in which the detector data are correlated with a bank of modeled waveforms (templates) that discretely cover the intrinsic parameter space, with each template representing a specific point in that space. The template bank is constructed such that, for any potential signal in the intrinsic parameter space, it contains at least one template within a distance $\mathcal{D}_{\rm max} = \sqrt{1 - \mathcal{M}_{\rm min}}$ determined by a chosen minimal match $\mathcal{M}_{\rm min}$. The value of $\mathcal{M}_{\rm min}$ sets the tradeoff between detection sensitivity and computational cost: a lower value permits larger mismatches between the signal and the nearest template, reducing the recovered signal-to-noise ratio (SNR) and hence the detection efficiency, whereas a higher value improves signal recovery at the expense of a larger number of templates and increased computational cost for both offline analyses and low-latency search pipelines. In this work, we adopt the standard choice of $\mathcal{M}_{\rm min} = 0.97$, which, under the usual scaling arguments, implies an expected loss of about 10% in detection rate due to the discrete coverage of the template bank [18].

Over the years, several approaches have been developed to make template bank generation as efficient as possible. Geometric methods based on lattice placement or metric tiling [18, 19] achieve near-optimal coverage when the parameter space is flat and low-dimensional. However, the intrinsic parameter space is not globally flat, and curvature effects introduce coverage gaps that require significant fine-tuning. This makes geometric methods difficult to generalize to higher dimensions, while the absence of a reliable metric for complex waveform models further restricts their applicability.

Stochastic methods [20, 21] provide a flexible alternative to geometric placement techniques. In their original bottom-up formulation, candidate templates are proposed sequentially, with the first proposal accepted immediately and each subsequent proposal added to the bank only if it lies at least $\mathcal{D}_{\rm max}$ away from all previously accepted templates. This process continues until the average acceptance ratio, computed over a fixed number of recent proposals, falls below a prescribed threshold, typically 10^{-4}.

An alternative stochastic-placement method, introduced in [22] as a top-down approach, begins with an oversampled proposal set $\mathcal{U}$ containing $|\mathcal{U}|$ candidate points distributed across the parameter space. Here $|\mathcal{U}|$ denotes the number of candidate points in the proposal set. The template bank is then constructed iteratively by selecting a point at random from $\mathcal{U}$, adding it to the bank $\mathcal{T}$, and removing all points lying within a distance

$\mathcal{D}_{\rm max}$ of the selected point. This procedure continues until $\mathcal{U}$ is exhausted. While the final template counts in the two approaches are nearly identical, the top-down method was shown in [22] to be approximately twice as fast. In either approach, the distance criterion may be evaluated using the parameter-space metric, when available, or through direct computation of the match between waveforms.

Finally, hybrid banks [22, 23] combine geometric placement with stochastic sampling to achieve more efficient template placement. In this geometric-random approach, one begins with an initial oversampled set of random proposals, $\mathcal{U}$, distributed across the parameter space. A randomly selected proposal is used as a seed, and only those neighboring points of an A_n^* lattice that lie within the prescribed search space are added to the template bank $\mathcal{T}$, under the assumption that the parameter space is locally flat. Redundant proposals in $\mathcal{U}$ lying within a distance $\mathcal{D}_{\rm max}$ of these accepted templates are discarded. This lattice-based expansion is repeated by treating each newly added template as a seed until no further valid lattice points can be added. The remaining proposals in $\mathcal{U}$, corresponding to regions not efficiently covered by the local geometric approximation owing to curvature in the parameter space or boundary effects, are then incorporated through the stochastic component of the algorithm.

In a naive implementation, the top-down stochastic algorithm can scale as $\mathcal{O}(N^2)$ in the worst case, since candidate rejection may require comparing selected templates with a large fraction of the proposal set. Tree-based implementations, such as KD-trees [24], substantially reduce this cost and typically give scaling closer to $\mathcal{O}(N \log N)$ for well-behaved point sets in moderate dimensions. Nevertheless, the size $N = |\mathcal{U}|$ of the initial proposal set remains a practical bottleneck, both in runtime and memory usage. This motivates the use of proposal strategies that reduce the required oversampling without compromising coverage.

The use of low-discrepancy sequences in this context was first explored by Manca & Vallisneri [25] in the framework of self-avoiding random coverings, where improved covering efficiency relative to uniform random sampling was demonstrated in flat Euclidean spaces. Here, we extend that idea to the construction of stochastic template banks for the intrinsic parameter space of compact binary gravitational-wave signals, where the underlying signal manifold is curved rather than flat.

We show that low-discrepancy sequences significantly reduce $|\mathcal{U}|$ while achieving recovery fractions comparable to those obtained using larger proposal sets generated from uniform random sampling. The use of LDS sampling also yields a modest reduction in the total number of templates, typically in the range $[-1.10,\ -0.42]\%$ in two dimensions and $[-1.12,\ -0.52]\%$ in three dimensions. These results demonstrate that for the parameter spaces studied here, comparable recovery fractions are obtained with 10–30% fewer proposal points.

Low-discrepancy sampling is not expected to significantly reduce the final template count for a fixed minimal match. The number of templates required to cover a parameter space is determined primarily by the metric volume of the signal manifold, the chosen minimal match, and the efficiency of the underlying covering. Instead, the principal

advantage of LDS lies in reducing the size $|\mathcal{U}|$ needed to achieve a given coverage. This reduction lowers memory requirements and improves the efficiency of nearest-neighbour searches used during stochastic bank construction, benefits that become increasingly important in higher-dimensional parameter spaces.

This paper is organized as follows. Sec. 2 provides a brief introduction to Low Discrepancy Sequences (LDS), covering their generation and their advantages for efficient space-filling. Sec. 3.1 reviews the metric on the signal manifold, establishing the notation used throughout the paper and introducing the key concepts. This sets the stage for Sec. 3.2, where we present the stochastic top-down algorithm employed in this work, along with key terminology such as fitting factors used in the subsequent analysis. Finally, Sec. 4 compiles the results by generating template banks across the parameter sets defined in Table 3, followed by a fitting factor study based on 10^5 random injections, with performance assessed via cumulative distribution functions (CDFs) of fitting factors. All analyses were performed using the `IMRPhenomD` waveform model [26], with the upper frequency cutoff set to the innermost stable circular orbit frequency $f_{\rm isco}$ corresponding to the total mass of the compact binary system.

2. LOW-DISCREPANCY SEQUENCES

In this section, we provide a brief overview of low-discrepancy sequences (LDS). These are deterministic sequences designed to sample a domain more uniformly than pseudo-random points. The first N elements of such a sequence define a proposal set with lower discrepancy than a typical pseudo-random sample of the same size, making them useful for generating well-distributed candidate points in stochastic template-bank construction.

These sequences have been extensively investigated and shown to be beneficial for Monte Carlo integration in higher dimensions compared to random uniform sampling.[27–29]. The two low-discrepancy sequences used in this paper are the *Halton* [30] and *Sobol* sequences [31]. Both can be viewed as extensions of the one-dimensional *van der Corput* sequence [32]. The construction begins by expressing a non-negative integer n in base b (usually a prime number) as $n = (\ldots d_4 d_3 d_2 d_1 d_0)_b$, or equivalently,

$$n = \sum_{k=0}^{m} d_k \, b^k. \tag{2.1}$$

The digits are then reversed with respect to the radix point to map the number into the unit interval, yielding $h = (0.d_0 d_1 d_2 d_3 \ldots)_b$. Accordingly, the n-th element of the van der Corput sequence in base b is given by

$$V(n, b) = \sum_{k=0}^{m} d_k \, b^{-(k+1)}. \tag{2.2}$$

A Halton sequence generalizes the one-dimensional van der Corput construction to higher dimensions by assigning each coordinate its own prime base: the first coordinate

uses base 2, the second base 3, the third base 5, and so on [30]. The n-th point of a two-dimensional Halton sequence is therefore $(h_2(n), h_3(n))$, where $h_b(n)$ is the radical-inverse function in base b, defined in Eq. (2.2). This function reverses the base-b digits of n and places them after the radix point, and Table 1 works through this digit-reversal explicitly for a few representative integers in bases 2 and 3.

n	Numerical Value	Mirrored Value	$h_b(n)$
Base(2) – For 1D (X-axis)			
1	$(1)_2 = 1 \times 2^0 = (1)_2$	$V(1,2) = (0.1)_2 = 1 \times 2^{-1}$	0.500
2	$(2)_2 = 1 \times 2^1 = (10)_2$	$V(2,2) = (0.01)_2 = 1 \times 2^{-2}$	0.250
6	$(6)_2 = 1 \times 2^1 + 1 \times 2^2 = (110)_2$	$V(6,2) = (0.011)_2 = 1 \times 2^{-2} + 1 \times 2^{-3}$	0.375
Base(3) – For 2D (Y-axis)			
4	$(4)_3 = 1 \times 3^0 + 1 \times 3^1 = (11)_3$	$V(4,3) = (0.11)_3 = 1 \times 3^{-1} + 1 \times 3^{-2}$	0.444
7	$(7)_3 = 1 \times 3^0 + 2 \times 3^1 = (21)_3$	$V(7,3) = (0.12)_3 = 1 \times 3^{-1} + 2 \times 3^{-2}$	0.556

Table 1. Illustration of the radical-inverse construction used in the Halton sequence. The first coordinate is obtained from the van der Corput sequence in base 2, while the second coordinate is obtained from the corresponding sequence in base 3.

Sobol sequences achieve low discrepancy through a different construction. Rather than assigning a distinct prime base to each dimension, they are built entirely in base 2, with each coordinate generated from a set of direction numbers specific to that dimension. This base-2 construction tends to produce more uniformly structured point sets as dimensionality increases, which is why Sobol sequences are often preferred in higher-dimensional applications. We use the Halton and Sobol implementations provided by SciPy throughout this work, and for a more detailed treatment of their construction we refer the reader to Ref. [33].

These quasirandom sequences are often *scrambled* [34, 35], meaning that deterministic or random permutations are applied to their digits in a way that preserves low discrepancy. Scrambling breaks unwanted structural correlations, so that the sequences behave like random samples while retaining their uniform space-filling properties.

To illustrate the space-filling advantage of LDS over uniform random sampling, we generate N points using uniform random, Halton, and Sobol sequences in 2D and 3D unit spaces, and track how coverage improves as N increases (Fig. 1). We quantify coverage by the covering radius r, defined as the largest distance from any point in the space to its nearest sample point. Intuitively, r is the radius of the largest empty ball that fits inside the sample, so it captures the worst-case gap in the coverage. In the context of gravitational-wave template bank generation, this quantity corresponds to the maximum mismatch, $r = \sqrt{1 - \mathcal{M}_{\rm min}}$. Operationally, for a bank of N points, we evaluate r by fixing 10,000 random test points and taking the maximum (over test points) of the distance to the nearest bank point. We then track how rapidly r falls below the threshold $r = \sqrt{1 - 0.97}$ as N grows, motivated by the minimal match $\mathcal{M}_{\rm min} = 0.97$ standard in gravitational-wave template bank searches. As shown in Fig. 1, both Halton and Sobol sequences reach this

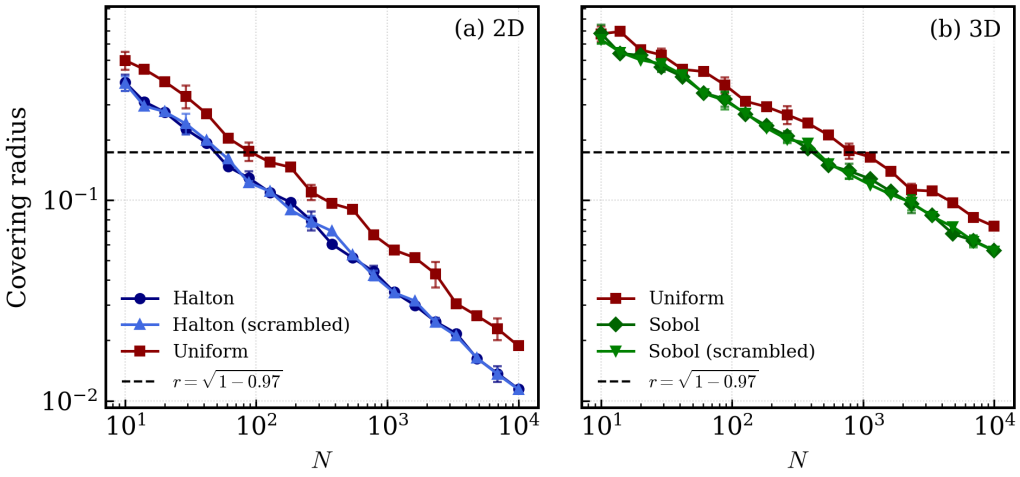

Figure 1. Scaling of the covering radius with N, for points placed in a unit space. Error bars are the standard deviation over multiple realizations. Low-discrepancy sequences (LDS) cross the threshold $r = \sqrt{1 - 0.97}$, with $\sim 40\%$ fewer proposals compared to uniform sampling, demonstrating more efficient space-filling.

threshold with approximately 40% fewer points than uniform random sampling, confirming their more efficient space-filling in the dimensionalities relevant here.

3. METHOD: TEMPLATE BANK CONSTRUCTION

3.1. Metric on the signal manifold

Template bank construction may be formulated as a covering problem on the signal manifold generated by a family of gravitational-wave templates.

We employ the `IMRPhenomD` [26] waveform model, whose frequency-domain representation may be written as

$$\tilde{h}(f; \vec{\lambda}, \vec{\xi}) = A(f; \vec{\lambda}, \vec{\xi})\, e^{-i\Psi(f; \vec{\lambda}, \vec{\xi})},$$

where $\vec{\lambda}$ and $\vec{\xi}$ denote the intrinsic and extrinsic parameters, respectively; A is the amplitude and Ψ is the phase of the waveform. For aligned-spin `IMRPhenomD` waveforms, the intrinsic parameter space consists of the component masses and the spin components aligned with the orbital angular momentum, i.e. $\vec{\lambda} = \{m_1, m_2, \chi_{1z}, \chi_{2z}\}$.

The local mismatch between nearby waveforms may be approximated using an intrinsic parameter-space metric g_{ij}. This metric is obtained by projecting the Fisher metric on the full signal manifold onto the intrinsic parameter subspace. Details of its construction are summarized in Appendix A. The mismatch neighbourhood of a template centred at $\vec{\lambda}_j$ is defined by

$$\Delta\vec{\lambda}^{\,T}\, g\, \Delta\vec{\lambda} \leq 1 - \mathcal{M}_{\rm min}, \tag{3.1}$$

where $\Delta\vec{\lambda} = \vec{\lambda} - \vec{\lambda}_j$ is the displacement to a neighbouring point in the intrinsic parameter space, and $\mathcal{M}_{\rm min}$ is the chosen minimal match. Eq. 3.1 defines the local region covered by

a template: once a proposal is accepted as a template, any remaining proposal satisfying this condition is removed because its predicted mismatch with the accepted template is no larger than $1 - \mathcal{M}_{\rm min}$. This is a covering criterion and does not impose a regular lattice spacing between accepted templates. The template-bank construction can therefore be viewed as a sphere-covering problem on this effective parameter space, where the goal is to cover the target region using the smallest possible set of metric spheres of radius $\mathcal{D}_{\rm max} = \sqrt{1 - \mathcal{M}_{\rm min}}$.

The use of the metric replaces expensive match evaluations with a local quadratic approximation to the waveform mismatch, thereby significantly reducing the computational cost of template-bank construction. In cases where the parameter-space metric is unavailable, distances between waveforms may instead be computed directly from overlap calculations.

For aligned-spin systems, it has been shown that the dominant spin effects may be captured by a single reduced-spin parameter $\chi_r = \chi_s + \delta\,\chi_a - (76\eta/113)\chi_s$, where χ_s and χ_a are the symmetric and antisymmetric spin combinations $(\chi_1 \pm \chi_2)/2$, $\eta = m_1 m_2/(m_1+m_2)^2$ is the symmetric mass ratio, and $\delta = (m_1 - m_2)/(m_1 + m_2)$ is the asymmetric mass ratio. This allows the four-dimensional intrinsic parameter space to be approximated by the three-dimensional manifold $\{m_1, m_2, \chi_r\}$ with minimal loss in effectualness [21].

This parameter space may be further reparametrized using the dimensionless chirp-time coordinates $(\theta_0, \theta_3, \theta_{3s})$. The transformation from (m_1, m_2, χ_r) to chirp-time coordinates yields a parametrization in which the metric components vary more slowly across the parameter space, making it particularly well suited for metric-based template placement. The dimensionless chirp-time coordinates are defined by

$$\theta_0 = \frac{5}{2^{1/3}} \left(\frac{1}{16\pi f_0 \eta m^{3/5}} \right)^{5/3}, \qquad \theta_3 = \left(\frac{16\pi^5 \theta_0^2}{25\eta^3} \right)^{1/5}, \qquad \theta_{3s} = \frac{48\pi}{113} \chi_r \theta_3. \tag{3.2}$$

where m denotes the total mass of the binary, and f_0 is the lower frequency cutoff. In this work, we construct 3D template banks over the intrinsic parameter space $(\theta_0, \theta_3, \theta_{3s})$ and 2D template banks over (θ_0, θ_3). In the latter case, the spin effects are neglected by setting $\theta_{3s} = 0$.

3.2. Template placement algorithm

Several techniques have been proposed for the placement of template banks in the intrinsic parameter space of compact-binary signals [20, 21, 36–39]. As discussed in Sec. 1, the stochastic template placement algorithm may be implemented in either a bottom-up or a top-down manner; we use the top-down approach, which begins from an oversampled proposal set and iteratively removes proposals already covered by a selected template, leaving the surviving selected points as the final bank.

We first generate a proposal set $\mathcal{U}$ in the intrinsic parameter space. In the standard stochastic approach this set is drawn from a uniform random distribution and oversampled to ensure adequate coverage; here we additionally compare this choice against proposal sets

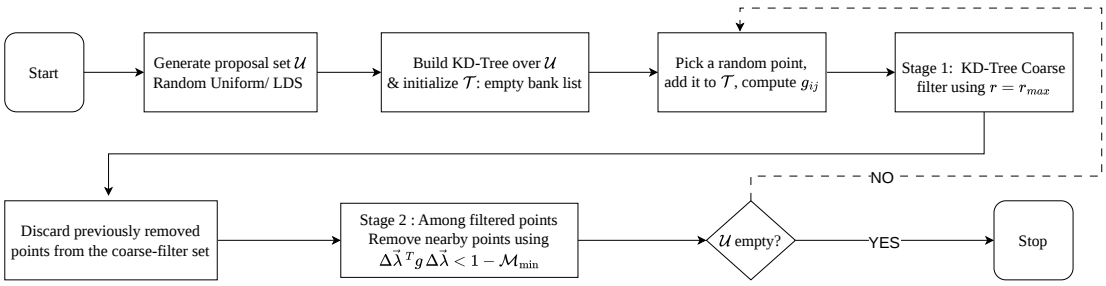

Figure 2. Flowchart for the top-down stochastic template bank construction algorithm. A proposal set $\mathcal{U}$ is generated once, using either traditional uniform random sampling or the LDS approach (proposed in this work), and a KD-tree is built over these points. At each iteration, a randomly chosen active proposal is promoted to the template list $\mathcal{T}$. Candidate neighbors of this proposal are first identified with a KD-tree broad query, then tested against the exact local metric condition. Covered proposals are marked inactive, and the process continues until no active proposals remain.

generated from low-discrepancy sequences (Halton and Sobol), which cover the parameter space more uniformly and can yield banks of comparable size and coverage from fewer initial proposals. To construct $\mathcal{U}$, we determine the allowed ranges of the chirp-time coordinates from the mass and spin ranges in Table 3, sample points over these coordinates, and map them back to physical masses and spins; only points satisfying the physical constraints and bounds of Table 3 are retained. Each point in $\mathcal{U}$ carries a Boolean active status, initially true for all proposals, and we initialize an empty template list $\mathcal{T}$. A Euclidean KD-tree is built once, using all points in $\mathcal{U}$, before the placement loop begins; points are never removed from the tree itself, only their active status is updated, thereby avoiding the cost of rebuilding it after every accepted template.

At each iteration, one active proposal $\lambda_j \in \mathcal{U}$ is chosen at random and promoted to $\mathcal{T}$, and the local parameter-space metric $g(\lambda_j)$ is computed at this point. A neighbouring proposal λ is covered by the template if the local quadratic mismatch condition, Eq. (3.1), is satisfied.

Diagonalizing the local metric, $g(\lambda_j) = Q\,\Lambda\,Q^T$, where the columns of Q are the eigenvectors q_k and $\Lambda = \mathrm{diag}(\alpha_1, \ldots, \alpha_n)$, Eq. (3.1) becomes

$$\sum_{k=1}^{n} \alpha_k\, u_k^2 \leq 1 - \mathcal{M}_{\rm min}, \tag{3.3}$$

in the metric eigenbasis, where $u_k = \Delta\lambda \cdot q_k$. The mismatch neighbourhood is thus an ellipsoid with principal axes aligned along q_k and semi-axis lengths

$$a_k = \sqrt{\frac{1 - \mathcal{M}_{\rm min}}{\alpha_k}}. \tag{3.4}$$

A small safety factor ϵ is applied in this coarse search, $\mathcal{M}_{\rm min} \to \mathcal{M}_{\rm min} - \epsilon$, giving enlarged semi-axes $a_k \to a_k^{(\epsilon)}$. Nevertheless, the final covering decision is always made using the exact threshold in Eq. (3.1).

Testing Eq. (3.1) against every active proposal in $\mathcal{U}$ is inefficient, so we first perform a coarse Euclidean search using the KD-tree. Let $\alpha_{\min}$ denote the minimum eigenvalue of $g(\lambda_j)$. Since

$$\alpha_{\min} \|\lambda - \lambda_j\|^2 \leq (\lambda - \lambda_j)^T \, g(\lambda_j) \, (\lambda - \lambda_j), \tag{3.5}$$

every point satisfying Eq. (3.1) must lie inside the Euclidean ball

$$\|(\lambda - \lambda_j)\| \leq r_{\max}, \tag{3.6}$$

where

$$r_{\max} = \sqrt{\frac{1 - \mathcal{M}_{\min}}{\alpha_{\min}}}. \tag{3.7}$$

This Euclidean ball of radius $r_{\max}$ is a conservative bounding region for the metric ellipsoid. Querying the KD-tree with this radius around λ_j returns a coarse candidate set containing all proposals that could possibly satisfy the covering condition, along with possibly many points outside the true ellipsoid when the local metric is anisotropic.

Since the query operates on the original set $\mathcal{U}$, returned candidates may include points already marked inactive in a previous iteration; these are discarded, and the remaining active candidates are tested against the exact condition, Eq. (3.1). All active proposals satisfying this condition, together with λ_j itself, are marked inactive. The algorithm then selects another random active point and repeats, terminating when no active proposals remain. At termination, every point in $\mathcal{U}$ is either included in the template bank or lies within the metric neighbourhood of a selected template. The final bank is the list $\mathcal{T}$.

This two-stage deletion procedure is illustrated in Fig. 2 and Fig. 3: a KD-tree broad query reduces the candidate set via a conservative Euclidean bound, followed by an exact metric cut that enforces the true local mismatch criterion.

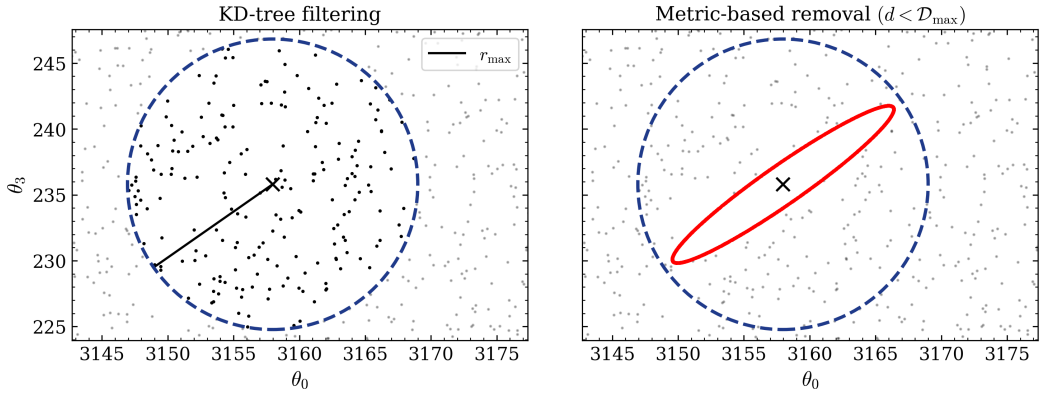

Figure 3. Illustration of the two-step point-deletion algorithm. The KD-tree filtering step, shown in the left panel, identifies proposals within the conservative bounding radius $r_{\max}$ of the reference template λ_{ref}; this radius is defined in Eq. (3.7). The surviving active proposals are then tested against the metric criterion, shown in the right panel. Points satisfying Eq. (3.1) are removed from the active proposal set $\mathcal{U}$.

Once a template bank $\mathcal{T}$ has been constructed, its effectiveness is assessed using random injections drawn from the same parameter space. For each injection we compute

the fitting factor [40], the maximum overlap between an arbitrary signal h_a and the templates h in the bank:

$$\mathcal{FF}(h_a) = \max_{h\in\mathcal{T}} \langle h_a \mid h\rangle. \tag{3.8}$$

Bank performance is evaluated via the cumulative distribution function of the fitting factors, together with the recovery fraction $\mathcal{R}_{0.97}$, defined as the percentage of injections with $\mathcal{FF} \geq 0.97$.

3.3. Slab-wise coarse filtering for anisotropic metrics

The induced metric g on the signal manifold is often highly anisotropic; the latter quantified by the condition number $\kappa(g) = \alpha_{\max}/\alpha_{\min}$, where $\alpha_{\max}$ and $\alpha_{\min}$ are the largest and smallest eigenvalues of $g(\lambda_j)$. For $\kappa \gg 1$, the metric ellipsoid is highly elongated. As a result, the conservative KD-tree selection around a chosen template over-approximates the true mismatch ellipsoid and returns a very large number of proposals that are subsequently rejected by the exact metric cut (see Fig. 4).

We therefore introduce an intermediate slab-wise coarse filtering step using the oriented bounding box of the metric ellipsoid as:

$$|\Delta\lambda \cdot q_k| \leq a_k^{(\epsilon)}, \qquad k = 1, \ldots, n. \tag{3.9}$$

Each inequality defines a slab bounded by two parallel hyperplanes normal to q_k. The oriented box is the intersection of these slabs. In practice, the slabs are applied sequentially, starting with the smallest semi-axis, so that the most restrictive directions reject candidates first. Since the KD-tree ball already enforces $\|\Delta\lambda\| \leq a_{\max}^{(\epsilon)}$, the widest slab is automatically satisfied by all KD-tree candidates and is therefore skipped while applying the slab cut.

Thus, each covering step in the template placement algorithm proceeds in three stages. First, the KD-tree is used to obtain a conservative Euclidean candidate set around the selected proposal. Second, this candidate set is further reduced using the slab-wise coarse filter, which keeps only points lying inside the oriented bounding box of the metric ellipsoid. Finally, the remaining candidates are tested using the exact quadratic metric condition. It is important to note that the slab-wise step is only a pre-filter to reduce the computational cost of each covering step; it does not change the active status of any proposal. A proposal is marked inactive only after it satisfies the final metric cut.

Figure 4 illustrates the KD-tree ball, slab-wise coarse filter, and exact metric neighbors in two dimensions.

The advantage of the slab filter is most apparent from candidate-count scaling. For a locally uniform proposal density ρ, the expected number of KD-tree candidates scales as the volume of the Euclidean bounding ball, $N_{\mathrm{KD}} \sim \rho V_n a_{\max}^n$, where V_n is the volume of the unit n-ball. On the other hand, the expected number of points inside the metric ellipsoid scales as $N_{\mathrm{exact}} \sim \rho V_n \prod_{k=1}^n a_k$. Thus

$$\frac{N_{\mathrm{KD}}}{N_{\mathrm{exact}}} \sim \frac{a_{\max}^n}{\prod_{k=1}^n a_k} \sim \sqrt{\frac{\prod_{k=1}^n \alpha_k}{\alpha_{\min}^n}}. \tag{3.10}$$

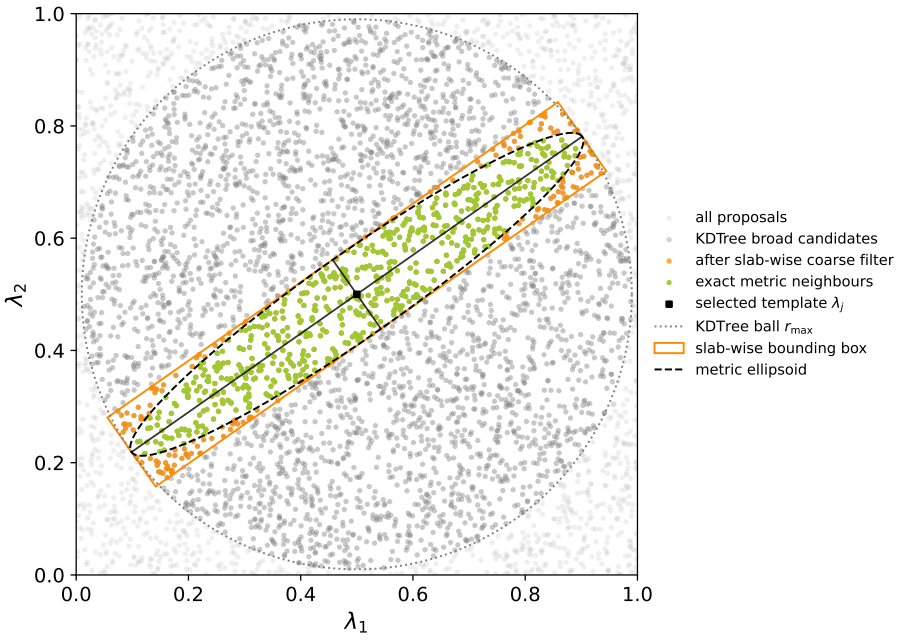

Figure 4. Illustration of the slab-wise coarse filtering step in two dimensions. The selected template is shown at λ_j, and $\Delta\lambda = \lambda - \lambda_j$. The KD-tree broad query first returns all proposals satisfying $\|\Delta\lambda\| \leq a^{(\epsilon)}_{\max}$. The slab-wise coarse filter then keeps only candidates inside the oriented bounding box defined by $|\Delta\lambda \cdot q_k| \leq a^{(\epsilon)}_k$ for each metric eigenvector q_k. Finally, the exact metric cut selects the proposals satisfying $\Delta\lambda^T g(\lambda_j)\Delta\lambda \leq 1 - \mathcal{M}_{\min}$.

This ratio grows rapidly with both dimension and anisotropy. The Euclidean KD-tree ball can therefore contain orders of magnitude more proposals than the actual metric neighbourhood.

By contrast, the slab-wise step replaces the Euclidean ball by an oriented box adapted to the metric eigenvectors. The box volume scales as $V_{\text{box}} = 2^n \prod_{k=1}^{n} a_k$, so that

$$\frac{N_{\text{box}}}{N_{\text{exact}}} \sim \frac{2^n}{V_n}. \tag{3.11}$$

This ratio is independent of metric anisotropy. The slab-wise filter in Eq. (3.9) is therefore better tailored to the geometry of the metric ellipsoid.

We tested the slab-wise coarse filter using a controlled local-query benchmark. We generated $N = 1.5 \times 10^6$ proposal points uniformly in the unit hypercube $[0, 1]^n$ for $n = 2$–6 and built a Euclidean KD-tree on each fixed proposal set, then selected 100 random query points. For each query point λ_j we assigned a synthetic positive-definite metric $g(\lambda_j) = Q\,\Lambda\,Q^T$, where Q is a random orthogonal matrix and the eigenvalues in Λ are logarithmically spaced between 1 and 10^4, giving a strongly anisotropic, randomly oriented metric ellipsoid with condition number $\kappa = 10^4$. The KD-tree broad-query radius was fixed to $r_{\max} = 0.25$. For each query we compared (a) the baseline consisting of the KD-tree broad query (Eq. (3.6)) followed directly by the exact metric cut (Eq. (3.1)) against (b) the slab-wise method, which applies the slab-wise coarse filter (Eq. (3.9)) before the exact

metric cut. We verified that both methods return the same final set of metric neighbours.

Results, averaged over the 100 queries, are summarized in Table 2. The slab-wise filter sharply reduces the number of candidates passed to the exact metric cut, and thus the number of full quadratic-form evaluations, with the benefit growing in higher dimensions: for $n > 3$ it cuts the local covering-step time by about 20–30% relative to the baseline.

4. RESULTS

In this section, we present the results for different template banks constructed in 2D and 3D using both random uniform sampling and low-discrepancy-sequence (LDS) sampling. Table 3 summarizes the parameter sets used to generate different banks. For generating the bank, we use the `IMRPhenomD` waveform model, and the `aLIGOZeroDetHighPower` [41] noise power spectral density (PSD) model.

The final template count in a top-down stochastic algorithm depends on $|\mathcal{U}|$ mainly before the proposal set is sufficiently oversampled. For small $|\mathcal{U}|$, parts of the parameter

n	N_{KD}	N_{slab}	N_{exact}	$N_{\mathrm{KD}}/N_{\mathrm{slab}}$	Speed-up
2	2.28×10^5	3.09×10^3	2.49×10^3	73.97	0.90
3	7.18×10^4	1.54×10^2	85.68	465.02	1.10
4	2.01×10^4	8.72	3.58	2303.05	1.23
5	4.92×10^3	1.35	1.03	3641.32	1.27
6	1.14×10^3	1.04	1.00	1096.61	1.33

Table 2. Local-query benchmark of the slab-wise coarse filtering step. The reported numbers are averages over random query points in an n-dimensional unit hypercube. Here N_{KD} is the average number of candidates returned by the KD-tree broad query, N_{slab} is the average number remaining after slab-wise coarse filtering, and N_{exact} is the average number satisfying the final metric cut. The slab-wise and direct pipelines were verified to return the same final set of metric neighbours. The speed-up is the ratio of the runtime of the baseline "KD-tree + exact-cut" method to that of the "KD-tree + slab-cut + exact-cut" method.

Bank Parameter	Set-I(2D)	Set-II(3D)
Waveform model	`IMRPhenomD`	`IMRPhenomD`
Noise model	`aLIGOZeroDetHighPower`	`aLIGOZeroDetHighPower`
Lower cut-off frequency f_{low}	20 Hz	20 Hz
Mass of first object m_1	$[1, 20]\, M_\odot$	$[1, 20]\, M_\odot$
Mass of second object m_2	$[1, 3]\, M_\odot$	$[1, 3]\, M_\odot$
Spin of first object χ_1	$--$	$[-0.98, 0.98]$
Spin of second object χ_2	$--$	$[-0.04, 0.04]$
Minimal Match M_{min}	0.97	0.97

Table 3. Different sets of parameters used to generate the banks. The parameter space for Set II is constructed by applying the NSBH mass boundary criterion, wherein objects having individual masses at or below $3\, M_\odot$ are treated as neutron stars, with their dimensionless spin magnitudes restricted to a range of ± 0.04.

space may be poorly sampled, leading to a smaller bank and a lower recovery fraction $\mathcal{R}_{0.97}$. As $|\mathcal{U}|$ increases, the recovery fraction improves and the final template count approaches a saturated value governed primarily by the metric volume and the chosen minimal match. We therefore determine the required size of $\mathcal{U}$ by studying the bank coverage as a function of $|\mathcal{U}|$ and selecting the point beyond which the improvement in coverage is negligible.

Set	Method	$\lvert\mathcal{U}\rvert$	$\langle n\rangle \pm \sigma$	$\mathcal{R}_{0.97} \pm \sigma$	$\Delta\mathcal{U}(\%)$	$\Delta n(\%)$
Set I	Random	400K	87549 ± 106	96.39 ± 0.07	—	—
	Halton-S	290K	86792 ± 103	96.46 ± 0.06	-27.5	$[-1.10, -0.63]$
	Halton	290K	86914 ± 159	96.42 ± 0.12	-27.5	$[-1.03, -0.42]$
Set II	Random	20000K	731830 ± 278	94.22 ± 0.04	—	—
	Sobol-S	17600K	725834 ± 1917	94.10 ± 0.06	-12.0	$[-1.12, -0.52]$
	Sobol	17600K	725263 ± 1107	94.13 ± 0.07	-12.0	$[-1.09, -0.71]$

Table 4. Comparison of stochastic template banks generated using uniform random sampling and LDS: Halton and Sobol over the parameter spaces defined in Table 3. Banks are constructed using 10 independent realizations of a fixed $|\mathcal{U}|$ and tested against a common set of 100,000 random injections per parameter space. Here, $\langle n\rangle \pm \sigma$ gives the mean and standard deviation of the number of templates, and $\mathcal{R}_{0.97} \pm \sigma$ denotes the mean recovery fraction above $\mathcal{FF} = 0.97$. The quantity $\Delta\mathcal{U}$ represents the percentage reduction in proposal set size relative to random uniform sampling. Δn gives the corresponding range in percentage reduction in template count, accounting for the $\pm\sigma$ uncertainties of both the LDS method and the random baseline. "S" denotes scrambled LDS.

For the 2D bank, we set $|\mathcal{U}| = 4 \times 10^5$, achieving a recovery fraction of around 96.39%. For the 3D bank placement, we set $|\mathcal{U}| = 2 \times 10^7$, which is consistent with the values used in Roy et al. [22] for the same parameter space. One practical way to choose $|\mathcal{U}|$ is first to estimate the total volume of the parameter space and use $\sim 1/10$ of that volume as an initial reference[22]. $|\mathcal{U}|$ can then be increased or decreased to this reference size until the desired recovery fraction is achieved. Any reduction in $|\mathcal{U}|$ without sacrificing recovery fraction directly translates into faster and more efficient bank generation. In addition, the memory footprint of the proposal set and the associated KD-tree [24] search structures also scale with $|\mathcal{U}|$, making reductions in $|\mathcal{U}|$ particularly valuable for higher-dimensional searches. To compare random and LDS sampling fairly, 10 independent realizations for fixed size of $\mathcal{U}$ are generated for each set given in Table 3 using random uniform sampling, and a bank is constructed from each realization. The corresponding recovery fractions are evaluated using a common set of 10^5 random injections drawn from the same parameter space. For LDS sampling, $|\mathcal{U}|$ is then adjusted until an average recovery fraction comparable to that of random uniform sampling is achieved.

In the 2D case, random uniform sampling achieves an average recovery fraction of $96.39 \pm 0.07\%$. Halton and scrambled Halton (Halton-S) sequences yield comparable or slightly higher recovery fractions of $96.42 \pm 0.12\%$ and $96.46 \pm 0.06\%$, respectively, while requiring 27.5% fewer proposal points. In the 3D case, random uniform sampling recovers $94.22 \pm 0.04\%$, whereas Sobol and scrambled Sobol (Sobol-S) sequences achieve comparable

recovery fractions of $94.13 \pm 0.07\%$ and $94.10 \pm 0.06\%$, respectively, with an approximately 12% reduction in $|\mathcal{U}|$.

Most Sobol realizations achieve recovery fractions comparable to random uniform sampling. A small number of realizations exhibit slightly lower recovery, increasing the spread across realizations and leading to a modest reduction in the average recovery fraction. This difference can be compensated by adding a small number of extra points to $\mathcal{U}$. As shown in Table 4, LDS sampling with $|\mathcal{U}| = 17600$K already approaches the random uniform coverage, and adding only 200–300K additional points would yield comparable or higher recovery fraction while still retaining a 12% reduction in $|\mathcal{U}|$.

The results for all LDS methods, together with the random uniform sampling reference, are summarized in Table 4. The corresponding cumulative distribution functions (CDFs) of the fitting factors are shown in Fig. 5.

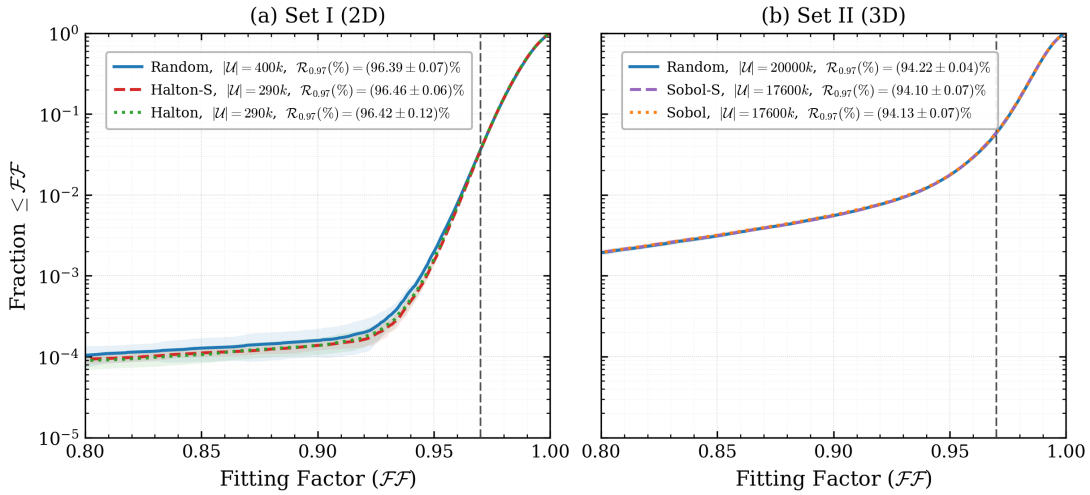

Figure 5. Cumulative distribution of the fitting factor $\mathcal{FF}$ for template banks constructed in Table 4, shown for Set I/2D (left) and Set II/3D (right). Each curve represents the mean CDF across 10 banks, constructed from 10 independent realizations of a fixed $|\mathcal{U}|$ and evaluated on a common set of 100,000 random injections per parameter space. The shaded band shows the $\pm\sigma$ across realizations. The vertical dashed line marks the minimal match threshold $\mathcal{FF} = 0.97$, above which the recovery fraction $\mathcal{R}_{0.97}$ is computed.

We find that LDS sampling is a more efficient way to generate proposals for the stochastic template-bank construction considered here. The final template count changes only marginally, by about 1% in both 2D and 3D, consistent with the fact that the bank size is mainly set by the metric volume of the target parameter space and the chosen minimal match.

The practical gain is instead in the size of the initial proposal set $\mathcal{U}$. With fewer points to store and process, LDS sampling reduces memory use, bookkeeping, and nearest-neighbour search overhead. To estimate the runtime impact, we measured the CPU time for one representative bank from each set in Table 3, using a single unloaded processor in a shared cluster environment.

For Set I (2D), a reduction of $\sim 4.5\%$ in CPU time is observed, with bank generation

taking 85.44 minutes for random uniform sampling, compared to 81.52 minutes for Halton and 81.50 minutes for scrambled Halton. In the higher-dimensional Set II (3D) case, the improvement is more pronounced, with a speed-up of $\sim 7\%$, reducing the runtime from 30.92 hours (random uniform) to 28.76 hours (Sobol) and 28.72 hours (scrambled Sobol). The observed speed-up arises primarily from the reduced proposal set size. Since the present study uses a computationally inexpensive metric approximation for match evaluation, even larger savings are expected in applications where matches must be computed explicitly through computationally expensive overlap integrals.

These results show that the main advantage of LDS sampling lies in the proposal stage: it reduces the number of initial points needed for comparable coverage, while the final bank size remains largely set by the metric volume and minimal match. The size of the numerical gain will depend on the waveform model, PSD, and parameter-space boundaries, but the reason for the improvement is generic to the method: better space filling than uniform random sampling.

5. DISCUSSION

We generated and tested several template banks in 2D and 3D and found that low-discrepancy sequence (LDS) sampling is more efficient for stochastic template placement than random uniform sampling. The main bottleneck in these stochastic algorithms is the size of the initial proposal set $\mathcal{U}$, and LDS sampling reduces the required $|\mathcal{U}|$ by approximately 27.5% in 2D and 12% in 3D. We also introduced a slab-wise coarse filtering strategy (Sec. 3.3) that accelerates candidate rejection for highly anisotropic metrics in higher-dimensional applications.

As expected, the final template count is only modestly reduced, by about 1% in both two and three dimensions since LDS sampling does not change the underlying geometry of the placement problem. At a fixed minimal match, the number of templates N needed to cover the n-dimensional intrinsic parameter space scales as

$$N \propto \frac{V_g}{(1 - \mathcal{M}_{\mathrm{min}})^{n/2}}, \tag{5.1}$$

where $V_g = \int \sqrt{|g|}\, d^n\lambda$ is the metric volume of the signal manifold and the proportionality constant depends on the placement algorithm's coverage efficiency. Since this scaling is set by the manifold geometry and the chosen minimal match, large reductions in bank size are not expected from LDS sampling alone.

The advantage of LDS sampling lies instead in shrinking the oversampled proposal set $\mathcal{U}$ needed for a given level of coverage. Because the memory footprint and computational cost of stochastic and hybrid placement algorithms are largely set by $\mathcal{U}$ and its associated search structures (e.g. KD-trees), a smaller $|\mathcal{U}|$ translates directly into lower memory use and faster bank construction. This benefit should grow in higher-dimensional spaces, where adequate coverage typically demands proposal sets far larger than the resulting bank.

LDS sampling could also be incorporated into existing hybrid placement methods, which combine top-down stochastic placement with lattice-based geometric placement

in locally flat regions but still typically begin from a uniformly sampled $\mathcal{U}$. Replacing this initial draw with an LDS proposal set could reduce $|\mathcal{U}|$ at comparable coverage, lowering memory and bookkeeping costs, with a possible small gain in final template count. This would be especially useful in optimized hybrid banks that rely on exact match calculations in parts of parameter space [23] – for instance high-mass binaries, where the metric approximation can underestimate the true mismatch neighbourhood, and a smaller proposal set means fewer expensive match evaluations when marking proposals inactive. Such savings should matter more for future searches with higher-dimensional waveform families, such as precessing and eccentric binaries, where uniform random proposal sets become increasingly inefficient.

Appendix A. Metric Calculation

In Section 3.1, we introduced the intrinsic parameter-space metric g_{ij} used for template-bank construction. We summarize its calculation for the `IMRPhenomD` waveform family.

The detector output may be regarded as a vector in a linear data space equipped with the noise-weighted inner product

$$\langle a|b\rangle = 4\,\mathrm{Re}\int_{f_{\mathrm{low}}}^{f_{\mathrm{high}}} \frac{\tilde{a}^*(f)\tilde{b}(f)}{S_n(f)}\,df, \tag{A.1}$$

where frequency bins are weighted by the noise power spectral density $S_n(f)$. For the metric calculations in this work, we take $f_{\mathrm{high}} = f_{\mathrm{ISCO}}$, the merger frequency of the binary, and use the `aLIGOZeroDetHighPower` noise power spectral density [41].
A family of normalized waveforms $\hat{h}(\lambda, \xi)$ forms a manifold embedded in this data space, where λ^i and ξ^μ are the intrinsic and extrinsic parameters. The overlap between two nearby waveforms is their match,

$$\mathcal{M} = \left\langle \hat{h}(\Theta)\middle|\hat{h}(\Theta+\Delta\Theta)\right\rangle, \tag{A.2}$$

with $\Theta^A = (\lambda^i, \xi^\mu)$. Expanding about the maximum at $\Delta\Theta^A = 0$, where the first derivatives vanish, gives

$$1-\mathcal{M} \simeq -\frac{1}{2}\left.\frac{\partial^2\mathcal{M}}{\partial\Delta\Theta^A\partial\Delta\Theta^B}\right|_{\Delta\Theta=0}\Delta\Theta^A\Delta\Theta^B. \tag{A.3}$$

The Hessian of the match at $\Delta\Theta = 0$ defines the Fisher matrix,

$$\Gamma_{AB} = -\left.\frac{\partial^2\mathcal{M}}{\partial\Delta\Theta^A\partial\Delta\Theta^B}\right|_{\Delta\Theta=0}, \tag{A.4}$$

equivalently, the curvature of the log-likelihood at its maximum. Since $\langle\hat{h}|\hat{h}\rangle = 1$ everywhere for normalized waveforms on the manifold, differentiating this normalization twice gives $\langle\hat{h}|\partial_A\partial_B\hat{h}\rangle = -\langle\partial_A\hat{h}|\partial_B\hat{h}\rangle$, so Eq. (A.4) becomes an inner product of waveform derivatives,

$$\Gamma_{AB} = \langle\partial_A\hat{h}|\partial_B\hat{h}\rangle. \tag{A.5}$$

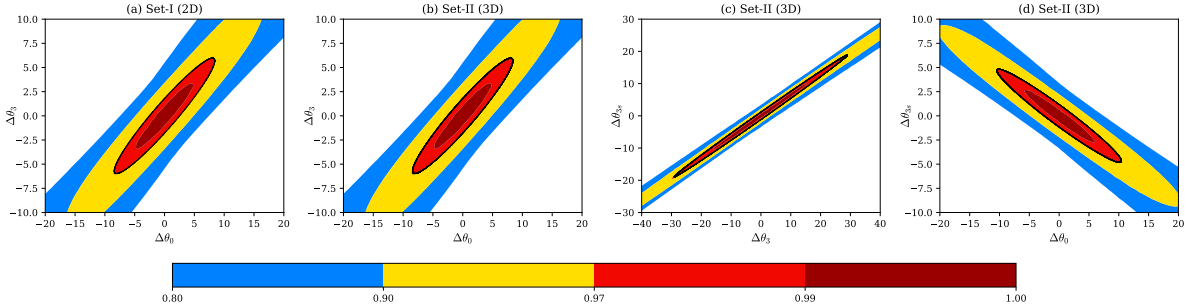

Figure A1. This figure compares the metric approximation with the exact match as defined in Eq. (A.2). Panels (a) show contours of the numerically computed exact match in the (θ_0, θ_3) plane at the central points of Set I(Table 3). Panels (b)–(d) show orthogonal slices of the exact-match contours in the three-dimensional parameter space $(\theta_0, \theta_3, \theta_{3s})$ at the center of Set II (Table 3). The corresponding metric ellipses are shown in black and are computed using Eq. (A.8). All black ellipses correspond to the contour at minimal-match $\mathcal{M}_{\rm min} = 0.97$.

Substituting Eq. (A.4) into Eq. (A.3),

$$1 - \mathcal{M} \simeq \frac{1}{2}\Gamma_{AB}\Delta\Theta^A\Delta\Theta^B. \tag{A.6}$$

Geometrically, Γ_{AB} is the pullback of the data-space metric, Eq. (A.1), onto the manifold of normalized waveforms. For frequency-domain waveforms of the form $\tilde{h}(f;\Theta) = A(f;\Theta)\, e^{-i\Psi(f;\Theta)}$, such as `IMRPhenomD` [26], this inner-product form reduces to

$$\Gamma_{AB} \simeq \frac{1}{\langle h|h\rangle}\left[\langle \partial_A A|\partial_B A\rangle + \langle A\,\partial_A\Psi|A\,\partial_B\Psi\rangle\right]. \tag{A.7}$$

Templates are placed only on the intrinsic parameters λ^i, so the extrinsic directions ξ^μ are projected out via the Schur complement of the extrinsic block. Additionally, by using Eq. (A.6) the resulting intrinsic mismatch metric is

$$g_{ij} = \frac{1}{2}\left(\Gamma_{ij} - \Gamma_{i\mu}\Gamma^{-1}_{\mu\nu}\Gamma_{\nu j}\right), \tag{A.8}$$

where i, j run over intrinsic and μ, ν over extrinsic parameters. The local mismatch between nearby templates then reduces to $1 - \mathcal{M} \simeq g_{ij}\Delta\lambda^i\Delta\lambda^j$, and this is the metric, Eq. (A.8), used for template-bank placement.

In Fig. A1, we illustrate the validity of this approximation is assessed by comparing the resulting metric ellipses with contours from exact match calculations, shown at a representative point in both the 2D and 3D parameter spaces. .

Acknowledgments

The authors thank Sudhir Gholap for carefully reading the manuscript and giving helpful suggestions to improve the presentation and clarity. We also thank Abhishek Sharma and

Divya Tahelyani for useful discussions and comments, and acknowledge support from IIT Gandhinagar, where the computations reported in this work were performed on the `noether` workstation of the Physics Department. Tarun Kumar would also like to thank Aayushi Jain, Akash Sahoo, and Ankit Mishra for their help during the initial stages of preparing the manuscript. Finally, the authors thank IIT Gandhinagar's computer support staff for their prompt assistance in resolving computing-related issues.

References

[1] J Aasi et al. Advanced LIGO. *Classical and Quantum Gravity*, 32(7):074001, Mar 2015. URL https://doi.org/10.1088/0264-9381/32/7/074001.

[2] F Acernese, M Agathos, K Agatsuma, et al. Advanced Virgo: a second-generation interferometric gravitational wave detector. *Classical and Quantum Gravity*, 32(2):024001, dec 2014. doi: 10.1088/0264-9381/32/2/024001. URL https://doi.org/10.1088/0264-9381/32/2/024001.

[3] Yoichi Aso, Michimura, et al. Interferometer design of the KAGRA gravitational wave detector. *Phys. Rev. D*, 88:043007, Aug 2013. doi: 10.1103/PhysRevD.88.043007. URL https://link.aps.org/doi/10.1103/PhysRevD.88.043007.

[4] B. P. Abbott et al. GW150914: First results from the search for binary black hole coalescence with Advanced LIGO. *Phys. Rev. D*, 93:122003, June 2016. doi: 10.1103/PhysRevD.93.122003. URL https://link.aps.org/doi/10.1103/PhysRevD.93.122003.

[5] LIGO Scientific Collaboration, Virgo Collaboration, and KAGRA Collaboration. GWTC-5.0: Observations from the Second Part of the Fourth LIGO-Virgo-KAGRA Observing Run and Updates to the Gravitational-Wave Transient Catalog. 2026.

[6] Sharan Banagiri, Christopher P. L. Berry, Cabourn Davies, et al. Unified $p_{\rm astro}$ for gravitational waves: Consistently combining information from multiple search pipelines. *Phys. Rev. D*, 108:083043, Oct 2023. doi: 10.1103/PhysRevD.108.083043. URL https://link.aps.org/doi/10.1103/PhysRevD.108.083043.

[7] M. Armano, H. Audley, J. Baird, et al. *LISA Pathfinder*, pages 185–204. doi: 10.1142/9789811207402_0013. URL https://www.worldscientific.com/doi/abs/10.1142/9789811207402_0013.

[8] Adrian Abac, Raul Abramo, Simone Albanesi, et al. The Science of the Einstein Telescope. *J. Cosmol. Astropart. Phys.*, 2026(03):081, March 2026. doi: 10.1088/1475-7516/2026/03/081. URL https://doi.org/10.1088/1475-7516/2026/03/081.

[9] Matthew Evans, Rana X. Adhikari, Chaitanya Afle, et al. A Horizon Study for Cosmic Explorer: Science, Observatories, and Community, 2021. URL https://doi.org/10.48550/arXiv.2109.09882.

[10] B. Iyer, T. Souradeep, C. S. Unnikrishnan, S. V. Dhurandhar, S. Raja, and A. S. Sengupta. LIGO-India: Proposal of the Consortium for Indian Initiative in Gravitational-wave Observations (IndIGO). Technical report, LIGO Scientific Collaboration, 2011. URL https://dcc.ligo.org/LIGO-M1100296/public. LIGO-M1100296-v2.

[11] M Saleem, Javed Rana, V Gayathri, et al. The science case for LIGO-India. *Classical and Quantum Gravity*, 39(2):025004, December 2021. ISSN 1361-6382. doi: 10.1088/1361-6382/ac3b99. URL http://dx.doi.org/10.1088/1361-6382/ac3b99.

[12] Sachin R. Shukla, Lalit Pathak, and Anand S. Sengupta. Pinpointing coalescing binary neutron star sources with the igwn, including ligo-aundha. *Phys. Rev. D*, 109:044051, Feb 2024. doi: 10.1103/PhysRevD.109.044051. URL https://link.aps.org/doi/10.1103/PhysRevD.109.044051.

[13] Abhishek Sharma, Divya Tahelyani, Anand S. Sengupta, and Sanjit Mitra. IndIGO-D: Probing Compact Binary Coalescences in the Decihertz GW Band, 1 2026. URL https://doi.org/10.48550/arXiv.2601.06956.

[14] B. P. Abbott et al. Observation of Gravitational Waves from a Binary Black Hole Merger. *Phys. Rev. Lett.*, 116:061102, Feb 2016. doi: 10.1103/PhysRevLett.116.061102. URL https://link.aps.org/doi/10.1103/PhysRevLett.116.061102.

[15] B. S. Sathyaprakash and S. V. Dhurandhar. Choice of filters for the detection of gravitational waves from coalescing binaries. *Phys. Rev. D*, 44:3819–3834, Dec 1991. doi: 10.1103/PhysRevD.44.3819. URL https://link.aps.org/doi/10.1103/PhysRevD.44.3819.

[16] Lee S. Finn. Detection, measurement, and gravitational radiation. *Phys. Rev. D*, 46:5236–5249, Dec 1992. doi: 10.1103/PhysRevD.46.5236. URL https://link.aps.org/doi/10.1103/PhysRevD.46.5236.

[17] S. V. Dhurandhar and B. S. Sathyaprakash. Choice of filters for the detection of gravitational waves from coalescing binaries. II. Detection in colored noise. *Phys. Rev. D*, 49:1707–1722, Feb 1994. doi: 10.1103/PhysRevD.49.1707. URL https://link.aps.org/doi/10.1103/PhysRevD.49.1707.

[18] Benjamin J. Owen and B. S. Sathyaprakash. Matched filtering of gravitational waves from inspiraling compact binaries: Computational cost and template placement. *Phys. Rev. D*, 60:022002, Jun 1999. doi: 10.1103/PhysRevD.60.022002. URL https://link.aps.org/doi/10.1103/PhysRevD.60.022002.

[19] T. Cokelaer. Gravitational waves from inspiralling compact binaries: Hexagonal template placement and its efficiency in detecting physical signals. *Phys. Rev. D*, 76:102004, Nov 2007. doi: 10.1103/PhysRevD.76.102004. URL https://link.aps.org/doi/10.1103/PhysRevD.76.102004.

[20] I. W. Harry, B. Allen, and B. S. Sathyaprakash. Stochastic template placement algorithm for gravitational wave data analysis. *Phys. Rev. D*, 80:104014, Nov 2009. doi: 10.1103/PhysRevD.80.104014. URL https://link.aps.org/doi/10.1103/PhysRevD.80.104014.

[21] P. Ajith, N. Fotopoulos, S. Privitera, A. Neunzert, N. Mazumder, and A. J. Weinstein. Effectual template bank for the detection of gravitational waves from inspiralling compact binaries with generic spins. *Phys. Rev. D*, 89:084041, Apr 2014. doi: 10.1103/PhysRevD.89.084041. URL https://link.aps.org/doi/10.1103/PhysRevD.89.084041.

[22] Soumen Roy, Anand S. Sengupta, and Nilay Thakor. Hybrid geometric-random template-placement algorithm for gravitational wave searches from compact binary coalescences. *Phys. Rev. D*, 95:104045, May 2017. doi: 10.1103/PhysRevD.95.104045. URL https://link.aps.org/doi/10.1103/PhysRevD.95.104045.

[23] Soumen Roy, Anand S. Sengupta, and Parameswaran Ajith. Effectual template banks for upcoming compact binary searches in Advanced-LIGO and Virgo data. *Phys. Rev. D*, 99:024048, Jan 2019. doi: 10.1103/PhysRevD.99.024048. URL https://link.aps.org/doi/10.1103/PhysRevD.99.024048.

[24] Jon Louis Bentley. Multidimensional binary search trees used for associative searching. *Communications of the ACM*, 18(9):509–517, 1975. doi: 10.1145/361002.361007. URL https://doi.org/10.1145/361002.361007.

[25] Gian Mario Manca and Michele Vallisneri. Cover art: Issues in the metric-guided and metric-less placement of random and stochastic template banks. *Phys. Rev. D*, 81:024004, Jan 2010. doi: 10.1103/PhysRevD.81.024004. URL https://link.aps.org/doi/10.1103/PhysRevD.81.024004.

[26] Sebastian Khan, Sascha Husa, Mark Hannam, Frank Ohme, Michael Pürrer, Xisco Jiménez Forteza, and Alejandro Bohé. Frequency-domain gravitational waves from nonprecessing black-hole binaries. ii. a phenomenological model for the advanced detector era. *Phys. Rev. D*, 93:044007, Feb 2016. doi: 10.1103/PhysRevD.93.044007. URL https://link.aps.org/doi/10.1103/PhysRevD.93.044007.

[27] Paolo Brandimarte. *Low-Discrepancy Sequences*, chapter 9, pages 379–401. John Wiley & Sons, Ltd, 2014. ISBN 9781118593264. doi: 10.1002/9781118593264.ch9. URL https://onlinelibrary.wiley.com/doi/abs/10.1002/9781118593264.ch9.

[28] Harald Niederreiter. *Random Number Generation and Quasi-Monte Carlo Methods*. SIAM, 1992. doi: 10.1137/1.9781611970081. URL https://doi.org/10.1137/1.9781611970081.

[29] Josef Dick and Friedrich Pillichshammer. *Digital Nets and Sequences: Discrepancy Theory and Quasi-Monte Carlo Integration*. Cambridge University Press, 2010. doi: 10.1017/CBO9780511761188. URL https://doi.org/10.1017/CBO9780511761188.

[30] J. H. Halton. On the efficiency of certain quasi-random sequences of points in evaluating multi-dimensional integrals. *Numerische Mathematik*, 2:84–90, 1960. doi: 10.1007/BF01386213. URL https://doi.org/10.1007/BF01386213.

[31] I.M Sobol. On the distribution of points in a cube and the approximate evaluation of integrals. *USSR Computational Mathematics and Mathematical Physics*, 7(4):86–112, 1967. ISSN 0041-5553. doi: https://doi.org/10.1016/0041-5553(67)90144-9. URL https://www.sciencedirect.com/science/article/pii/0041555367901449.

[32] J. G. van der Corput. Verteilungsfunktionen i. *Proceedings of the Koninklijke Nederlandse Akademie van Wetenschappen*, 38:813–821, 1935. URL https://www.dwc.knaw.nl/DL/publications/PU00018547.pdf.

[33] Ishaan L. Dalal, Deian Stefan, and Jared Harwayne-Gidansky. Low Discrepancy Sequences for Monte Carlo Simulations on Reconfigurable Platforms. In *2008 International Conference on Application-Specific Systems, Architectures and Processors (ASAP)*, pages 108–113, July 2008. doi: 10.1109/ASAP.2008.4580163. URL https://doi.org/10.1109/ASAP.2008.4580163.

[34] Art B. Owen. Scrambling Sobol and Niederreiter–Xing Points. *Journal of Complexity*, 14 (4):466–489, 1998. ISSN 0885-064X. doi: https://doi.org/10.1006/jcom.1998.0487. URL https://www.sciencedirect.com/science/article/pii/S0885064X98904873.

[35] Abdalla G. M. Ahmed, Matt Pharr, and Peter Wonka. ART-Owen Scrambling. *ACM Trans. Graph.*, 42(6), December 2023. ISSN 0730-0301. doi: 10.1145/3618307. URL https://doi.org/10.1145/3618307.

[36] Chad Hanna, James Kennington, Shio Sakon, et al. Binary tree approach to template placement for searches for gravitational waves from compact binary mergers. *Phys. Rev. D*, 108:042003, Aug 2023. doi: 10.1103/PhysRevD.108.042003. URL https://link.aps.org/doi/10.1103/PhysRevD.108.042003.

[37] Keisi Kacanja, Alexander H. Nitz, Shichao Wu, Marco Cusinato, Rahul Dhurkunde, Ian Harry, Tito Dal Canton, and Francesco Pannarale. Efficient stochastic template bank using inner product inequalities. *The Astrophysical Journal*, 975(2):212, Nov 2024. doi: 10.3847/1538-4357/ad7d87. URL https://doi.org/10.3847/1538-4357/ad7d87.

[38] Duncan A. Brown, Ian Harry, Andrew Lundgren, and Alexander H. Nitz. Detecting binary neutron star systems with spin in advanced gravitational-wave detectors. *Phys. Rev. D*, 86: 084017, Oct 2012. doi: 10.1103/PhysRevD.86.084017. URL https://link.aps.org/doi/10.1103/PhysRevD.86.084017.

[39] Collin Capano, Ian Harry, Stephen Privitera, and Alessandra Buonanno. Implementing a search for gravitational waves from binary black holes with nonprecessing spin. *Phys. Rev. D*, 93:124007, Jun 2016. doi: 10.1103/PhysRevD.93.124007. URL https://link.aps.org/doi/10.1103/PhysRevD.93.124007.

[40] Theocharis A. Apostolatos. Search templates for gravitational waves from precessing, inspiraling binaries. *Phys. Rev. D*, 52:605–620, Jul 1995. doi: 10.1103/PhysRevD.52.605. URL https://link.aps.org/doi/10.1103/PhysRevD.52.605.

[41] David Shoemaker. Advanced LIGO Anticipated Sensitivity Curves. Technical Report LIGO-T0900288-v2, LIGO Laboratory, 2010. URL https://dcc.ligo.org/LIGO-T0900288-v2/public.